Advanced Composites and Hybrid Materials (2023) 6:5
https://doi.org/10.1007/s42114-022-00580-6

RESEARCH

# Synergetic effect of Ni-Au bimetal nanoparticles on urchin-like $TiO_2$ for hydrogen and arabinose co-production by glucose photoreforming

**Malin Eqi[1,2] · Cai Shi[1,2] · Jiajing Xie[3,4] · Fuyan Kang[1,2] · Houjuan Qi[1,2] · Xushen Tan[1,2] · Zhanhua Huang[1,2] · Junli Liu[5] · Jiang Guo[3]**

Received: 3 September 2022 / Revised: 2 November 2022 / Accepted: 7 November 2022 / Published online: 7 December 2022


## Abstract

Biomass photoreforming is a prospective and attractive strategy to kill two birds with one stone for not only producing hydrogen ($H_2$) but also valorizing biomass by exploiting infinite solar energy. Here, we design Ni-Au bimetal nanoparticles modified urchin-like $TiO_2$ photocatalysts (NiAu/$TiO_2$) and demonstrate an enhanced glucose photoreforming. The $H_2$ production rate of the optimal $Ni_{0.05}Au_{0.45}/TiO_2$ (6391.86 μmol $h^{-1}$ $g^{-1}$) is 118.57, 30.78, and 1.65 times of pure $TiO_2$ (53.91 μmol $h^{-1}$ $g^{-1}$), $Ni_{0.5}/TiO_2$ (207.56 μmol $h^{-1}$ $g^{-1}$), and $Au_{0.5}/TiO_2$ (3867.12 μmol $h^{-1}$ $g^{-1}$), respectively. Meanwhile, the glucose conversion rate and the corresponding arabinose selectivity over $Ni_{0.05}Au_{0.45}/TiO_2$ are up to 95.00% and 36.54% after 4-h photoreforming, which are higher than the corresponding monometallic and pristine $TiO_2$. The synergistic effect of Ni and Au nanoparticles, including the localized surface plasmon resonance (LSPR) and Schottky junction of Au nanoparticles and the promoting effect of Ni particles on C–C cleavage in glucose, as well as the three-dimensional hierarchical urchin-like $TiO_2$, significantly improve the $H_2$ production, glucose conversion, and arabinose selectivity. The research paves a new way to the great potential of bimetal nanoparticles in biomass photoreforming.

**Keywords** Ni-Au bimetal nanoparticles (NPs) · Urchin-like $TiO_2$ · Glucose photoreforming · Arabinose · $H_2$ production

## 1 Introduction

There is a growing interest in exploiting the "biorefinery" platform for the production of sustainable chemicals and fuels instead of century-old petroleum refineries [1]. However, traditional biomass biorefinery platform technologies, such as thermochemical (e.g., combustion, gasification, and pyrolysis) and bioprocesses (e.g., microbial fermentation and enzymatic digestion), are facing setbacks at current stage due to the carbon-intensive process and high capital cost [2]. The photoreforming of biomass and its derivatives into high-value chemicals and hydrogen ($H_2$) is an emerging strategy for alleviating the present fossil fuel shortage crisis, global warming, and environmental pollution [3–5].

Glucose, the fundamental unit of cellulose, is the most widely investigated model substrates for biomass photoreforming in the past four decades [6]. It can be transferred to 5-hydroxymethylfural, arabinose, and formic acid during the photoreforming process [7–9]. Among them, arabinose has attracted much attention because of its wide applications in biological, chemical, and medical fields. Extraction of arabinose from some natural plants is a possible way, but

Malin Eqi and Cai Shi contributed equally to this work.

✉ Zhanhua Huang
huangzh1975@163.com

✉ Junli Liu
liujunli1974@126.com

✉ Jiang Guo
jguo@sust.edu.cn

1 Key Laboratory of Bio-Based Material Science & Technology, Material Science and Engineering College, Northeast Forestry University, Harbin 150040, China

2 Engineering Research Center of Advanced Wooden Materials, Ministry of Education, Northeast Forestry University, Harbin 150040, China

3 School of Materials Science and Engineering, Shaanxi Key Laboratory of Green Preparation and Functionalization for Inorganic Materials, Shaanxi University of Science & Technology, Xi'an 710021, China

4 College of Materials Science and Engineering, Taiyuan University of Science and Technology, Taiyuan, China

5 Institute of Chemical Industry of Forest Products, CAF. Key Laboratory of Biomass Energy and Material, Nanjing 21004, Jiangsu Province, China

the limitation is its high cost and the complex purification procedures [10]. Directly converting glucose to arabinose via the photoreforming by the controlled C1-C2 bonds scission is a prospective strategy using oxidizing active species such as holes ($h^+$) [11]. Nevertheless, the low selectivity of arabinose as a result of the over-oxidation of glucose is still challenging [12]. Consequently, it is still urgent to design photocatalysts with controllable oxidation capacity and corresponding catalytic system to obtain high efficiency hydrogen ($H_2$) and high selectivity chemicals simultaneously.

Titania ($TiO_2$) has been widely investigated in biomass photoreforming because of its suitable conduction band and valence band position, as well as the corrosion resistance, nontoxic, and low cost [12–14]. However, the wide band gap and high photogenerated electron–hole pairs ($e^-$-$h^+$) recombination rate of conventional $TiO_2$ usually lead to a low photoreforming efficiency [15]. Recently, Hu et al. proved that gold nanoparticles decorated three dimensionally ordered macropore $TiO_2$ (3DOM $TiO_2$-Au) can dramatically improve glucose conversion and arabinose selectivity [4]. And Surawut et al. also demonstrated that Ag-doped $TiO_2$ nanofibers have excellent recycling ability with high-performance photoreforming glucose ability due to the localized surface plasmon resonance (LSPR) of Ag NPs [16]. Furthermore, Hynd et al. demonstrated that Ni−Pd bimetallic NPs deposited on $TiO_2$ (Ni−Pd/$TiO_2$) can minimize the cost of catalyst and increase the $H_2$ production activity [17]. The modification of Au nanoparticles (NPs) with LSPR effect and high work function can significantly facilitate the separation of $e^-$-$h^+$ and visible light absorption ability in $TiO_2$ [4, 18]. In addition, considering the potential of Ni NPs also with high work function in C–C bond cleavage ($Ni_\Phi = 5.3$ eV) [19–21], depositing Ni-Au bimetal NPs not only improved the photoreforming activity, but also minimized the cost. This has been demonstrated to be an excellent option to increase the performance of photoreforming [17, 22]. Besides, it is worth mentioning that the effective contact between photocatalysts and glucose substrates can promote mass diffusion between these two, which is especially important for biomass photoreforming. Three-dimensional (3D) hierarchically structure favors facilitating the mass diffusion based on Murray's law [23]. Depositing Ni-Au bimetal on 3D hierarchically urchin-like $TiO_2$ is a promising strategy for minimizing costs as well as maximizing the photoreforming activity.

Here, Ni-Au bimetal NPs modified 3D hierarchically urchin-like $TiO_2$ photocatalysts ($Ni_xAu_{0.5-x}/TiO_2$) were designed and their application for $H_2$ and arabinose co-generation by glucose photoreforming was demonstrated. $Ni_xAu_{0.5-x}/TiO_2$ exhibited excellent $H_2$ production accompanied by arabinose production activity. Under the optimized reaction condition, the $H_2$ production rate of $Ni_{0.05}Au_{0.45}/TiO_2$ (6391.86 μmol $h^{-1}$ $g^{-1}$) was 118.57, 30.78, and 1.65 times of pure $TiO_2$ (53.91 μmol $h^{-1}$ $g^{-1}$), $Ni_{0.5}/TiO_2$ (207.56 μmol $h^{-1}$ $g^{-1}$), and $Au_{0.5}/TiO_2$ (3867.12 μmol $h^{-1}$ $g^{-1}$), respectively. Meanwhile, the glucose conversion rate and the corresponding arabinose selectivity over $Ni_{0.05}Au_{0.45}/TiO_2$ were up to 95.00% and 36.54% after 4-h photoreforming. The photoreforming mechanism was also investigated by means of photoelectrochemistry and carrier dynamics.

## 2 Experimental

### 2.1 Reagents and instruments

The information of reagents and instruments were showed in supporting material.

### 2.2 Preparation of photocatalyst

#### 2.2.1 Synthesis of 3D hierarchically urchin-like $TiO_2$

The 3D hierarchically urchin-like $TiO_2$ (abbreviated as $TiO_2$) was synthesized according to our previous work through a one-step hydrothermal method. In details, acetone (3 mL) and titanium tetrachloride (0.5 mL) were added into a sample bottle with ultrasonic treatment for half an hour. Then, the sample bottle containing the above solution was placed in a Teflon-lined autoclave, and heated from an ambient temperature to 135 °C and kept for 48 h. Finally, the samples were collected by cooling the Teflon-lined autoclave to an ambient temperature, collecting the sediment by rinsing and centrifuging before drying it under 60 °C for 10 h.

#### 2.2.2 Synthesis of $Au_xNi_{0.5-x}/TiO_2$

A series of $Ni_xAu_{0.5-x}/TiO_2$ ($x = 0$, 0.05, and 0.5 wt%) were synthesized via impregnation method. Firstly, 0.2 g $TiO_2$ was suspended in 5.5 mL of $Ni(NO_3)_2$ (0.001 mol $L^{-1}$) and 26.5 mL of $HAuCl_4$ (0.001 mol $L^{-1}$) solution with magnetic agitation for 1 h. Then, 0.1 mol $L^{-1}$ L-Lysine was added into the above mixture. After that, 5 mL newly prepared $NaBH_4$ solution was added dropwise into it with stirring for another 10 min. The suspension was experimentally aged under an ambient temperature for 24 h. Finally, the catalyst was gathered by centrifugation and drying. The formation process of $Ni_xAu_{0.5-x}/TiO_2$ ($x = 0$, 0.05, 0.15, and 0.25) is schematically described in Scheme 1.

### 2.3 Photocatalytic activity test

Typically, 25 mg of the prepared photocatalyst, 31.8 mg of $Na_2CO_3$ and 0.05 g glucose were dispersed into 50 mL aqueous solution containing 25 mL water and 25 mL $CH_3CN$. The suspension was vacuumed for 0.5 h to remove the

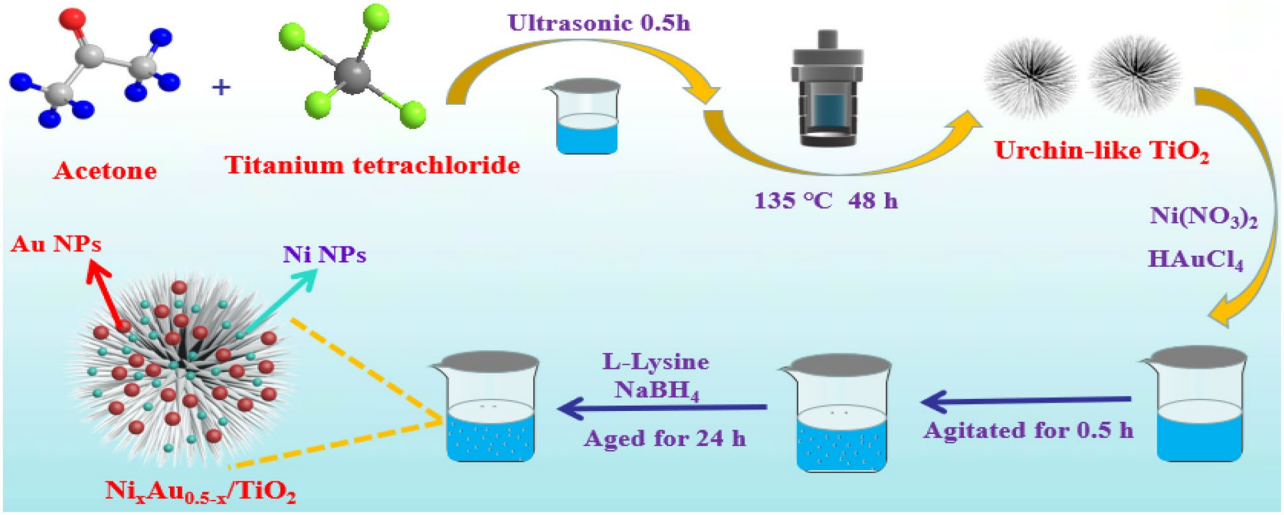


**Scheme 1** Scheme presentation of the synthetic route of $Ni_xAu_{0.5-x}/TiO_2$

existing gas before illumination. The temperature was controlled at 6 °C by circulating condensation. Then, the system was irradiated by a 300 W Xe-lamp under magnetically stirring. The evolved $H_2$ gas was automatically quantitatively analyzed every 0.5 h during 4 h photoreforming process by gas chromatography with a thermal conductive detector. High-performance liquid chromatography was carried to determine liquid products. Glucose and arabinose were detected by using a 1260 ELSD detector with a mobile phase of $CH_3CN$ and aqueous solution containing 0.3% ammonium hydroxide in a volume ratio of 8:2 with a flow rate of 0.5 mL $min^{-1}$. The column temperature was set at 40 °C.

## 3 Results and discussion

### 3.1 Photocatalyst structure characteristics

To investigate the morphology and microstructure of $Ni_{0.05}Au_{0.45}/TiO_2$, FESEM and HRTEM were performed. FESEM images showed that 3D hierarchically urchin-like $TiO_2$ microspheres with a diameter of around 6 μm were composed of one-dimensional (1D) nanorods (Fig. 1a, b). HRTEM image further verified this point (Fig. 1c). Some studies have shown that this special 3D hierarchical structure is conducive to mass transfer in the biomass reforming process [4, 23]. HRTEM image of $Ni_{0.05}Au_{0.45}/TiO_2$ in Fig. 1d indicated that $TiO_2$ still maintained complete 3D hierarchical urchin-like morphology after impregnation. HRTEM images of $Ni_{0.05}Au_{0.45}/TiO_2$ exhibited that Au and Ni NPs around 5 nm were well deposited on $TiO_2$ nanorods, and the shorter distance between Au and Ni NPs played a vital role for their coordination. Also, both Au and Ni NPs were in a tight contact with the $TiO_2$ nanorods (Fig. 1e, f), which was favorable for the effective photogenerated carriers. The measured lattice spacings of 0.204 and 0.233 nm corresponded to Ni (111) facet and Au (111) facet, respectively [24, 25]. Furthermore, EDS mapping also presented that the Au and Ni NPs were homogeneously distributed throughout the $TiO_2$ sample (Fig. 1g–j), and the EDS spectrum shown in Fig. 1k further verify the successful loading of Au and Ni NPs on $TiO_2$.

As shown in Fig. 2a, the crystallinity and crystallographic phases of $Ni_xAu_{0.5-x}/TiO_2$ were analyzed by pXRD. The diffraction peaks located at $2\theta = 27.35°$, 35.86°, 41.05°, 43.83°, 54.11°, 56.42°, 63.82°, and 69.57° could be attributed to (110), (101), (111), (210), (211), (220), and (301) lattice planes of rutile $TiO_2$ [26]. Meanwhile, the observed weak diffraction peaks at $2\theta = 62.63°$ and 68.73° were indexed to the anatase $TiO_2$ (204) and (116) planes [15], respectively. The diffraction peaks (Fig. 2a) of Au NPs possessed four peaks at $2\theta = 77.34°$, 64.76°, 44.10°, and 38.18°corresponding to (311), (220), (200), and (111) planes, respectively [27]. It was worth noting that Au (200) plane was indistinguishable because of its overlapping with the (210) plane of rutile $TiO_2$. Moreover, the diffraction peaks related to Ni NPs were not observed in the pXRD patterns of $Ni_xAu_{1-x}/TiO_2$, which might be attributed to the high dispersity of Ni NPs on $TiO_2$, as shown in EDS mapping (Fig. 1j) [28] or to the content below the detection limit [29]. Interestingly, the peak at 27.35° of $TiO_2$ shifted to little lower angles slightly after the deposition of metals NPs (in inset in Fig. 2a). This kind of offset phenomenon could be explained by the integration of Ni-Au bimetal NPs with $TiO_2$, particularly for $TiO_2$ with $e^-$-rich oxygen vacancy ($O_v$) sites [24]. The existence of lattice defects ($O_v$ sites) was conductive to the

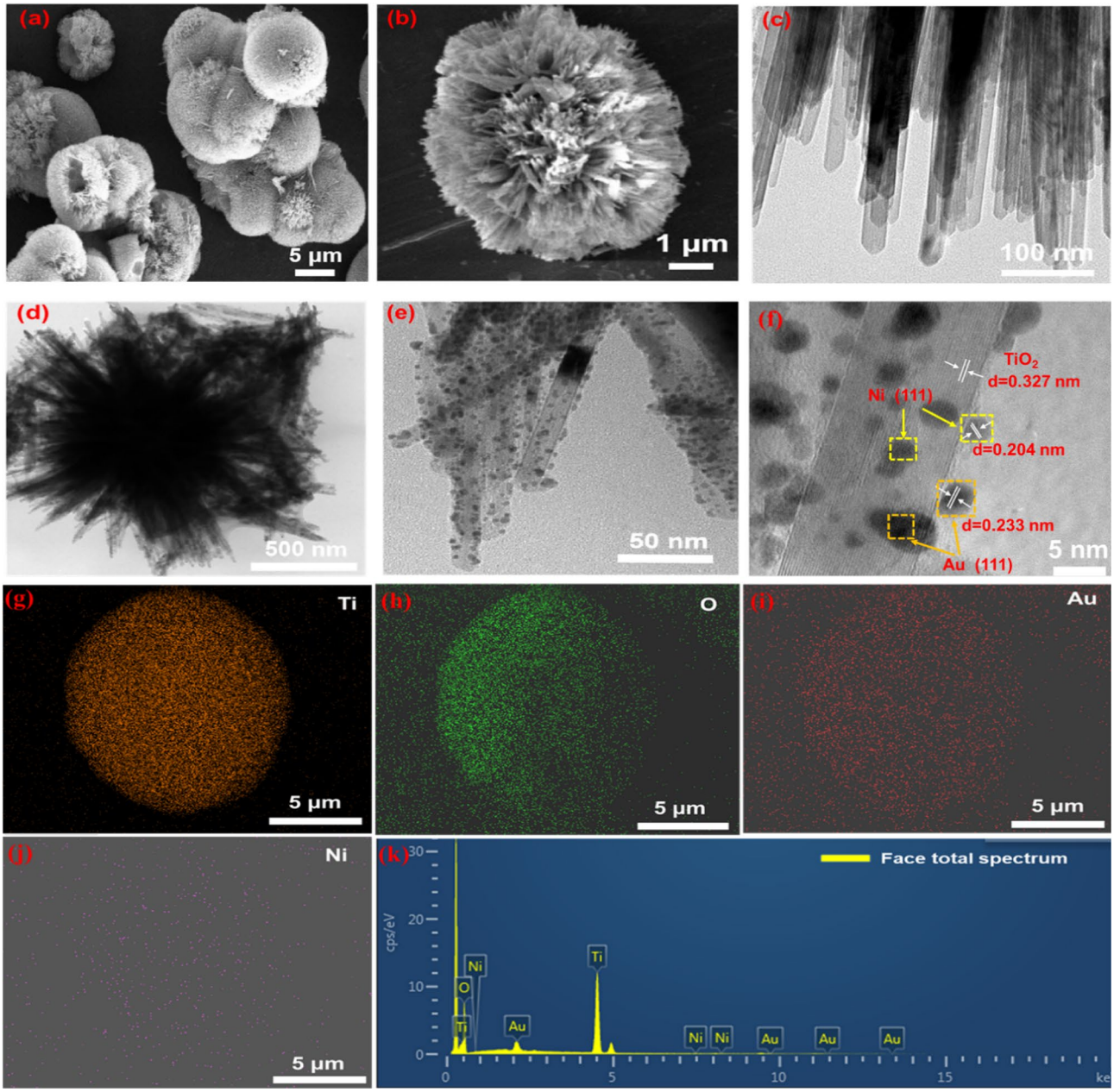


**Fig. 1** **a**, **b** FESEM images of $TiO_2$. **c** HRTEM image of $TiO_2$. **d**, **e**, **f** TEM and HRTEM images of $Ni_{0.05}Au_{0.45}/TiO_2$. **g–k** Elements mapping and EDS of Ti, O, Au, and Ni in $Ni_{0.05}Au_{0.45}/TiO_2$

interaction between the Ti lattice and metal NPs, so that the Ni-Au bimetal NPs could be better dispersed on the surface of $TiO_2$ (Fig. 2i, j) [24, 30–34].

XPS was performed to analyze the surface elemental compositions as well as the chemical states of $Ni_{0.05}Au_{0.45}/TiO_2$ (Fig. 2c–f). Figure 2b revealed the existence of C, O, Ni, Ti, and Au elements. The C 1 s peak could be ascribed to adventitious carbon [35]. The Ti 2p image depicted in Fig. 2c exhibited four peaks of $Ti^{4+}$ $2p_{1/2}$, $Ti^{3+}$ $2p_{1/2}$, $Ti^{4+}$ $2p_{3/2}$, and $Ti^{3+}$ $2p_{3/2}$ located at 464.4, 463.5, 458.9, and 458.0 eV, respectively. As shown in Fig. 2d, the O1s peaks at 529.9, 530.4, and 531.6 eV corresponded to the O atoms in Ti–O, -OH, and $O_v$ neighbors to $Ti^{3+}$, respectively [15, 36–38]. The existence of $O_v$ in $TiO_2$ facilitated visible light absorption and charge separation simultaneously [39–45]. The peaks at 86.9 and 83.3 eV were assigned to Au $4f_{5/2}$ and Au $4f_{7/2}$of $Au^0$ (Fig. 2e) [28, 46]. In the Ni 2p spectrum in Fig. 2f, a signal peak of $Ni^0$ $2p_{3/2}$ peak was identified at 852.9 eV, which revealed the existence of $Ni^0$ [17]. The peaks at 863.4 and 855.7 eV belonged to Ni $2p_{1/2}$ and

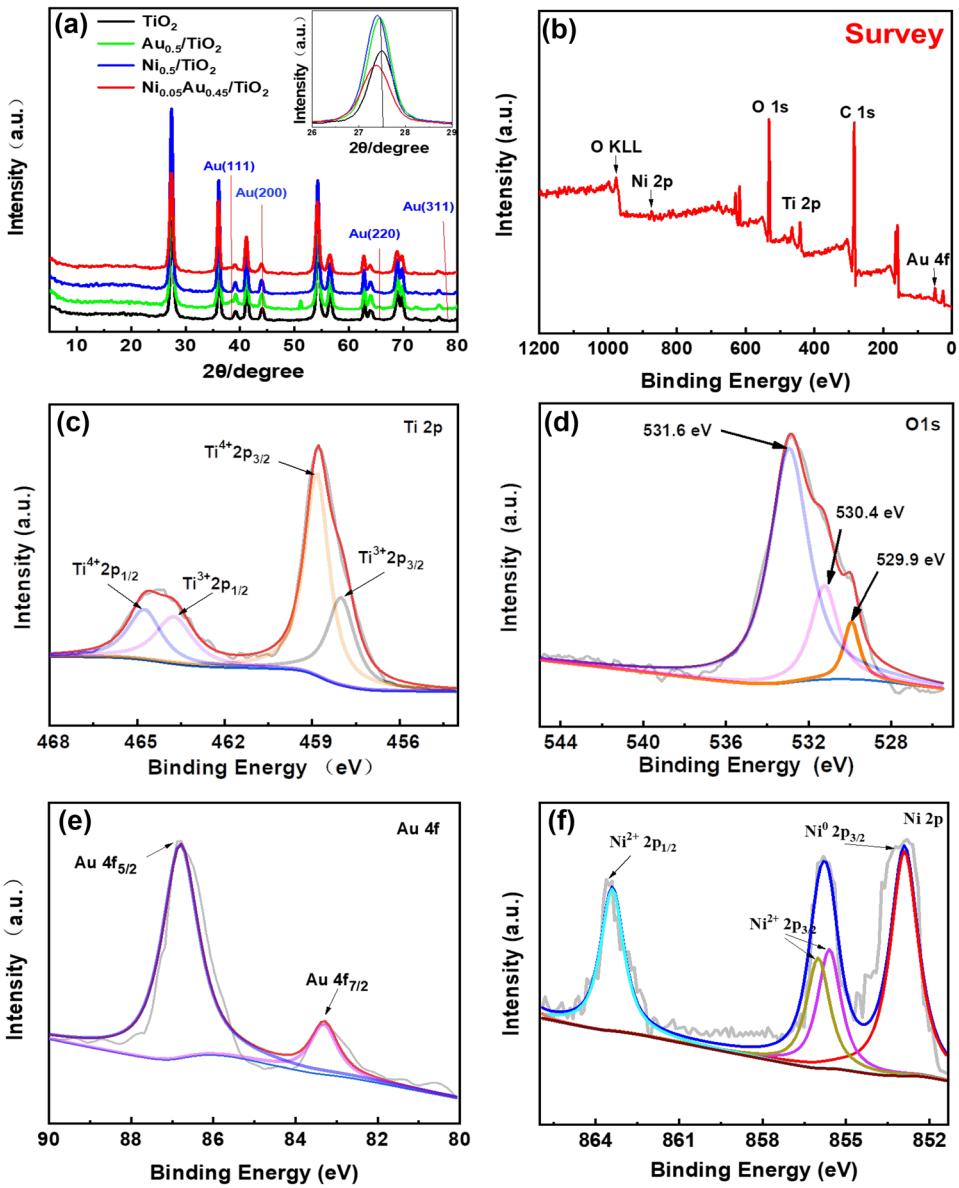


**Fig. 2** **a** pXRD patterns of $Ni_xAu_{0.5-x}/TiO_2$ (inset displays magnified angles from 26° to 29°). **b–f** The high-resolution XPS spectra of survey, O 1 s, Ti 2p, Au 4f, and Ni 2p in $Ni_{0.05}Au_{0.45}/TiO_2$

Ni $2p_{3/2}$ of $Ni^{2+}$, respectively, which proved the presence of NiO in $Ni_{0.05}Au_{0.45}/TiO_2$ [17]. Since the Ni species was very sensitive to oxygen, exposing Ni to air might cause the partially oxidization of Ni NPs into NiO clusters during the drying process. The above analysis showed that $Au^0$, $Ni^0$ and NiO coexist in $Ni_{0.05}Au_{0.45}/TiO_2$, which is beneficial to the subsequent biomass photoreforming reaction.

The effective contact between photocatalysts and glucose substrates can promote mass diffusion, which was an important point in biomass photoreforming. Therefore, the $N_2$ adsorption–desorption isotherms (at 77 K) were performed to determine the specific surface. Meanwhile, the pore-size distributions of $Ni_xAu_{0.5-x}/TiO_2$ were conducted to determine the pore volumes. As displayed in Figs. S1-S2, all tested photocatalysts showed a type IV isotherms with H3 hysteresis loop, and the pore size ranged from 2 to 38 nm [15, 47]. Tables S1 and S2 show that the deposition of Ni-Au bimetals NPs had no significant effect on the specific surface area and pore volume of $TiO_2$ itself, and they still retained perfect 3D hierarchically urchin-like morphology, as indicated by HRTEM in Fig. 1d.

## 3.2 Optical and photoelectrical properties

The optical characteristics of $TiO_2$ and $Ni_xAu_{0.5-x}/TiO_2$ were analyzed by UV–vis DRS (Fig. 3a, b). An absorption band edge of $TiO_2$ appeared at about 424 nm because of the doping of $Ti^{3+}$ in it. $Ni_{0.5}/TiO_2$ showed a flat absorption within the visible region because of the d-d transition

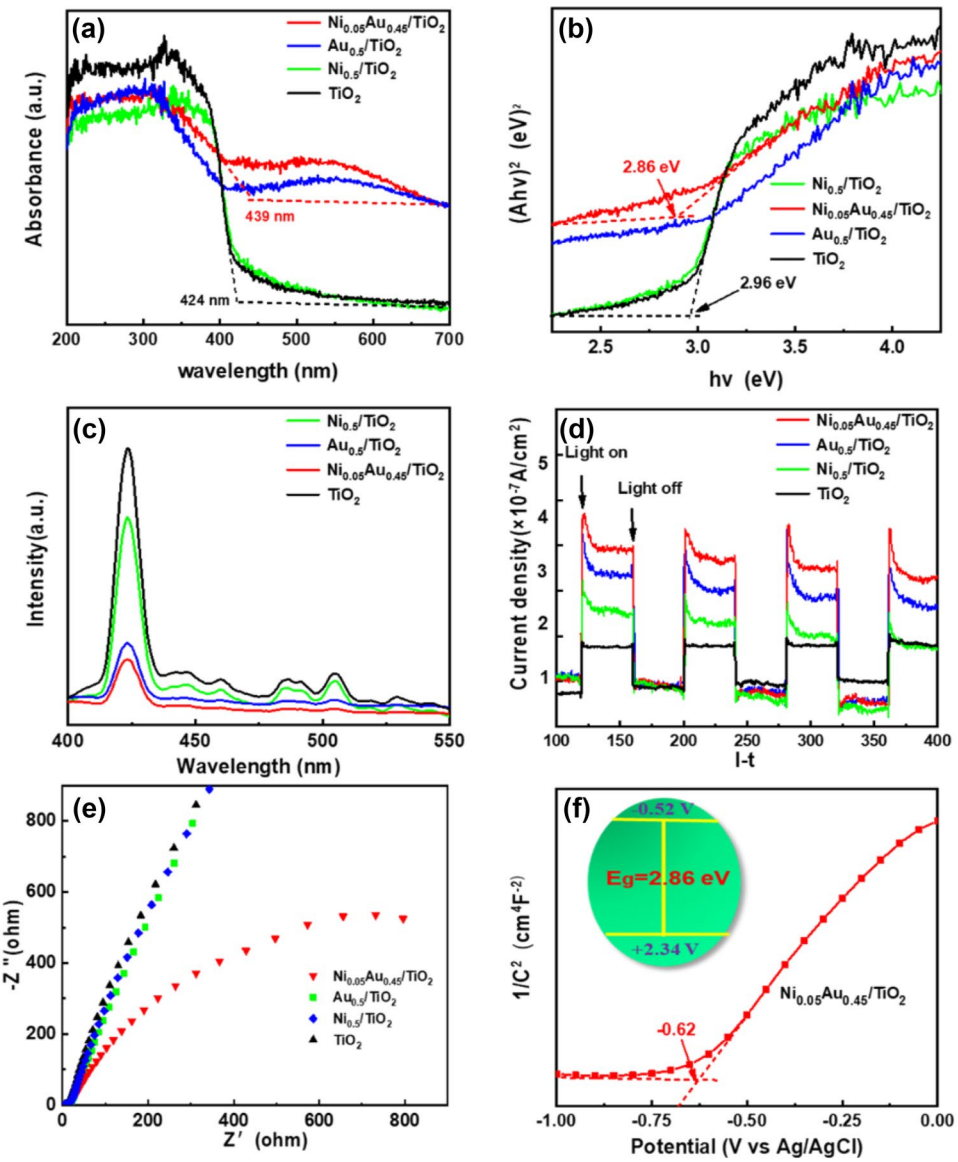


**Fig. 3** **a** UV–vis DRS, **b** the corresponding bandgap energy, **c** PL spectra, **d** transient photocurrent response, and **e** Nyquist plot of $TiO_2$ and $Ni_xAu_{0.5-x}/TiO_2$. **f** Mott-Schottky plot of $Ni_{0.05}Au_{0.45}/TiO_2$ (inset in Fig. 4f shows the energy band structure of $Ni_{0.05}Au_{0.45}/TiO_2$)

in NiO [48]. $Au_{0.5}/TiO_2$ demonstrated an obvious absorption band edge redshift and an extra extended, and reinforced visible light absorption around 480–630 nm, which was caused by the localized surface plasmon resonance (LSPR) of Au NPs [17, 49]. The UV–vis DRS spectrum of $Ni_{0.05}Au_{0.45}/TiO_2$ was consistent with that of $Au_{0.5}/TiO_2$. This indicated that no alloy was formed between the Au and Ni NPs, which were independent and relatively close to each other, as displayed in Fig. 1f. Moreover, the Kubelka–Munk method was adopted to calculate the equivalent bandgaps ($E_g$) by the following equations (Eqs. (1), (2), (3), and (4)) [50]. And the $E_g$ of the $Ni_{0.05}Au_{0.45}/TiO_2$ was calculated to be 2.86 eV (Fig. 3b).

$$\frac{K}{S} = \frac{\left(1 - R_\infty\right)^2}{2R_\infty} = F\left(R_\infty\right) \tag{1}$$

$$R_\infty = \frac{R_{\text{sample}}}{R_{\text{standard}}} \tag{2}$$

$$\alpha hv = B\left(hv - E_g\right)^n \tag{3}$$

Putting $F(R_\infty)$ instead of $\alpha$ into Eq. (3) yields the form:

$$\left(F\left(R_\infty\right)hv\right)^n = B\left(hv - E_g\right) \tag{4}$$

where $S$ is scattering coefficient, $K$ is absorption coefficient, $R_\infty$ is the diffuse reflectance, $F(R_\infty)$ is Kubelka–Munk function, $\alpha$ is linear absorption coefficient, $v$ is light frequency, $A$ is proportionality constant, and $n$ is taken equal to the 1/2 for direct band gap materials [50].

The role of loading Au-Ni bimetal NPs in alleviating the recombination of photogenerated $e^-$-$h^+$ was surveyed

by photoluminescence (PL) spectra. As presented in Fig. 3c and S4, all PL emission spectra of $Ni_xAu_{0.5-x}/TiO_2$ exhibited similar positions to that of bare $TiO_2$ at 469 nm, which was induced by the deep energy level emission of the typical structural defects ($O_v$) existing in the photocatalysts [51]. It was clearly observed that the PL emission intensity of $Ni_{0.05}Au_{0.45}/TiO_2$ was dramatically decreased compared with other samples, which manifested that the introduction of Ni-Au bimetal NPs would highly improve the separation efficiency of the photoexcited charges carriers. It was speculated that the excited $e^-$ might migrate from the conduction band of $TiO_2$ to the Ni-Au bimetal NPs due to the high work function of Ni and Au NPs [29], which could promote the transition and separation of the charge carriers, then distinctly prolonged the reactive lifetimes of the photogeneration carries. This was also beneficial to the enhancement of photoreforming activity.

To validate the influence of Ni-Au bimetal NPs on promoting the photoexcited charge carrier separation, transient photocurrent and EIS were conducted (Fig. 3d, e). All the catalysts showed reproducible and relatively stable photocurrent throughout the chopped on/off light cycles (Fig. 3d). Among them, $Ni_{0.05}Au_{0.45}/TiO_2$ showed the highest photocurrent density, which proved that the deposition of Ni-Au bimetal NPs on $TiO_2$ could significantly improve the photocurrent density of $TiO_2$ [52–55]. The semi-circular signal of the EIS was employed to evaluate the charge transfer resistance (Fig. 3e) [56]. In normal conditions, the charge transfer resistance of the surface was equal to the diameter of the semi-circular part of the Nyquist diagram, a shorter radius corresponds to a smaller surface charge transfer resistance [57]. It was obvious that the $Ni_{0.05}Au_{0.45}/TiO_2$ exhibited the lowest charge transfer resistance as well as the optimal photo-induced $e^-$-$h^+$ separation efficiency.

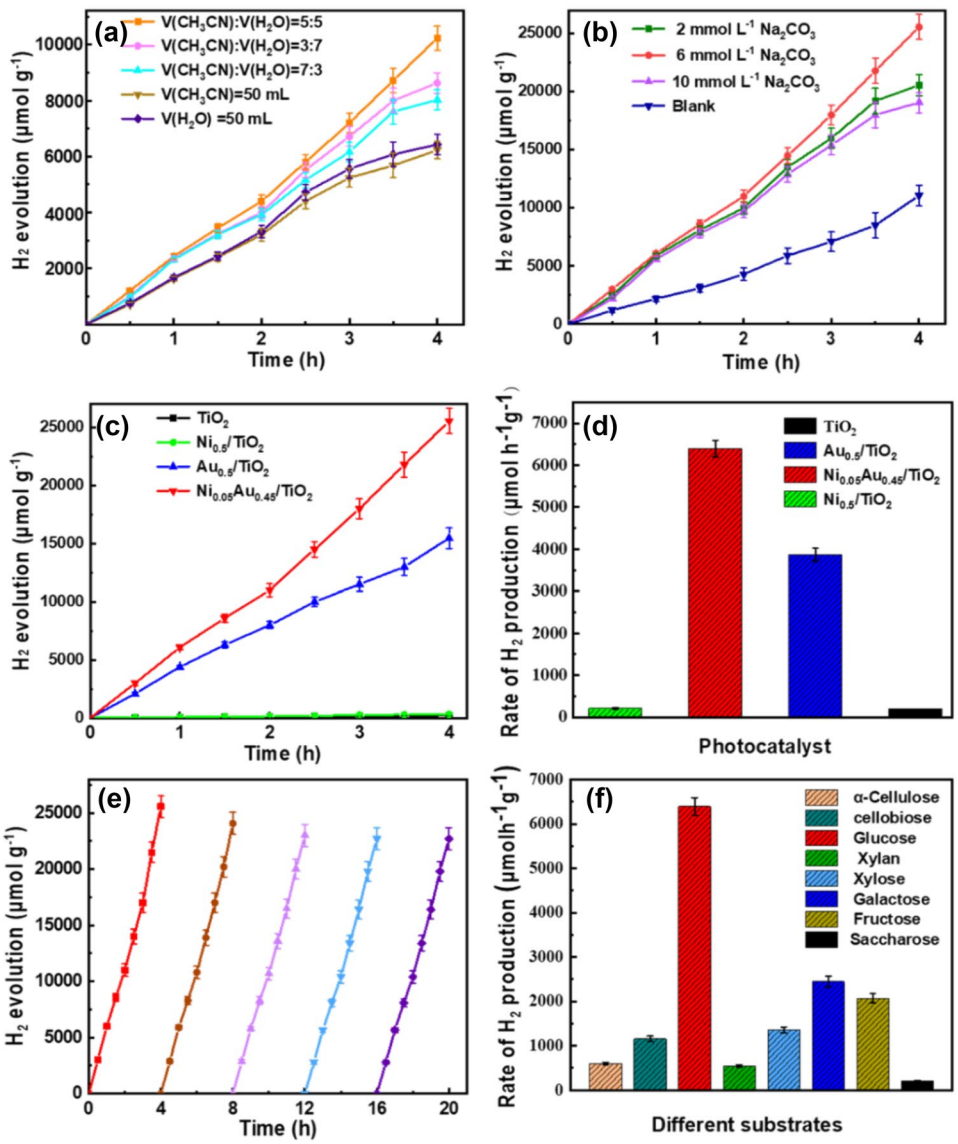


**Fig. 4** **a** The $H_2$ evolution amount of the $Ni_{0.05}Au_{0.45}/TiO_2$ in solvent with different ratios of $CH_3CN$ and $H_2O$. **b** The $H_2$ evolution amount of the $Ni_{0.05}Au_{0.45}/TiO_2$ in different $Na_2CO_3$ concentrations (the ratio of $CH_3CN$ and $H_2O$ was 1:1). **c**, **d** The $H_2$ evolution from glucose photoreforming for different catalysts. **e** Long time recycling test of the optimal system for $H_2$ evolution from glucose photoreforming. **f** The $H_2$ evolution rate of the optimal system from different biomass derivatives. The reaction condition of **c**, **d**, **e**, and **f**: 25 mg catalyst, 25 mL $H_2O$, 25 mL $CNCH_3$, 6 mmol $L^{-1}$ $Na_2CO_3$, 50 mg glucose, 300 W Xenon lamp

Afterwards, the Mott-Schottky (M-S) plot (Fig. 3f) was measured to determine the electronic band structure of the $Ni_{0.05}Au_{0.45}/TiO_2$. The positive slope on the M-S plot of $Ni_{0.05}Au_{0.45}/TiO_2$ revealed that $Ni_{0.05}Au_{0.45}/TiO_2$ had a n-type semiconductor characteristic. The *x*-axis intercept of M-S plot revealed the flat band potential ($E_{fb}$) of semiconductor electrode [58]. Figure 3f shows that the $E_{fb}$ of $Ni_{0.05}Au_{0.45}/TiO_2$ was −0.62 eV (vs. Ag/AgCl). The flat band potential ($E_{fb}$) was somewhere around 0.1 eV lower than the corresponding conduction band ($E_{CB}$) for the most n-type semiconductors [59]. The corresponding $E_{CB}$ value of $Ni_{0.05}Au_{0.45}/TiO_2$ was equivalent to −0.52 eV (vs. NHE). And as described above in Fig. 3b, the $E_g$ value was calculated to be 2.86 eV of $Ni_{0.05}Au_{0.45}/TiO_2$. Therefore, it could be determined that the $E_{VB}$ value $Ni_{0.05}Au_{0.45}/TiO_2$ is to be +2.34 eV (vs. NHE) based on the equation of $E_g = E_{VB} - E_{CB}$. The electronic energy band structure of $Ni_{0.05}Au_{0.45}/TiO_2$ was drawn in the inset of Fig. 3f.

### 3.3 $H_2$ evolution from photoreforming glucose

The photoreforming $H_2$ production performance of various photocatalysts ($TiO_2$ and $Ni_xAu_{0.5-x}/TiO_2$) was tested, with glucose as a model substrate. The effects of different conditions on the photocatalytic $H_2$ production by $Ni_{0.05}Au_{0.45}/TiO_2$ were first investigated (Fig. 4a, b and S3). It was clear that the $H_2$ release rate was the highest when the volume ratio of $CH_3CN$ and $H_2O$ was 1:1 ($CH_3CN$ 25 mL, $H_2O$ 25 mL). On this basis, the addition of $Na_2CO_3$ further improved the $H_2$ production (Fig. 4b). This might be because the addition of $CH_3CN$ made the resulting liquid product more conducive to separation and did not cover the catalyst active sites. Adding $Na_2CO_3$ (soluble base) highly improved the glucose photooxidation efficiency [60]. All subsequent photocatalytic reactions were proceeded under the optimal condition. As shown in Fig. 4c, the $H_2$ accumulation of photocatalyst increased with time from the glucose photoreforming without any trend of slowing down after 4 h reaction. The calculated $H_2$ release rate of $TiO_2$ was approximately 53.91 μmol $h^{-1}$ $g^{-1}$ (Fig. 4d). The $H_2$ generation efficiency of $TiO_2$ could be attributed to the $O_v$ introduced by $Ti^{3+}$ doping and the sufficient contact between the photocatalyst and the glucose substrate due to the unique 3D hierarchical urchin-like morphology without any co-catalyst. However, the $H_2$ production efficiency of pristine $TiO_2$ was far lower than any of $Ni_xAu_{0.5-x}/TiO_2$ (*x* = 0, 0.05, and 0.5), especially for $Ni_{0.05}Au_{0.45}/TiO_2$. The $H_2$ production activity of $Ni_{0.05}Au_{0.45}/TiO_2$ could reach 6391.86 μmol $h^{-1}$ $g^{-1}$, which was 118.57, 30.78, and 1.65 times than that of pure $TiO_2$ (53.91 μmol $h^{-1}$ $g^{-1}$), $Ni_{0.5}/TiO_2$ (207.56 μmol $h^{-1}$ $g^{-1}$), and $Au_{0.5}/TiO_2$ (3867.12 μmol

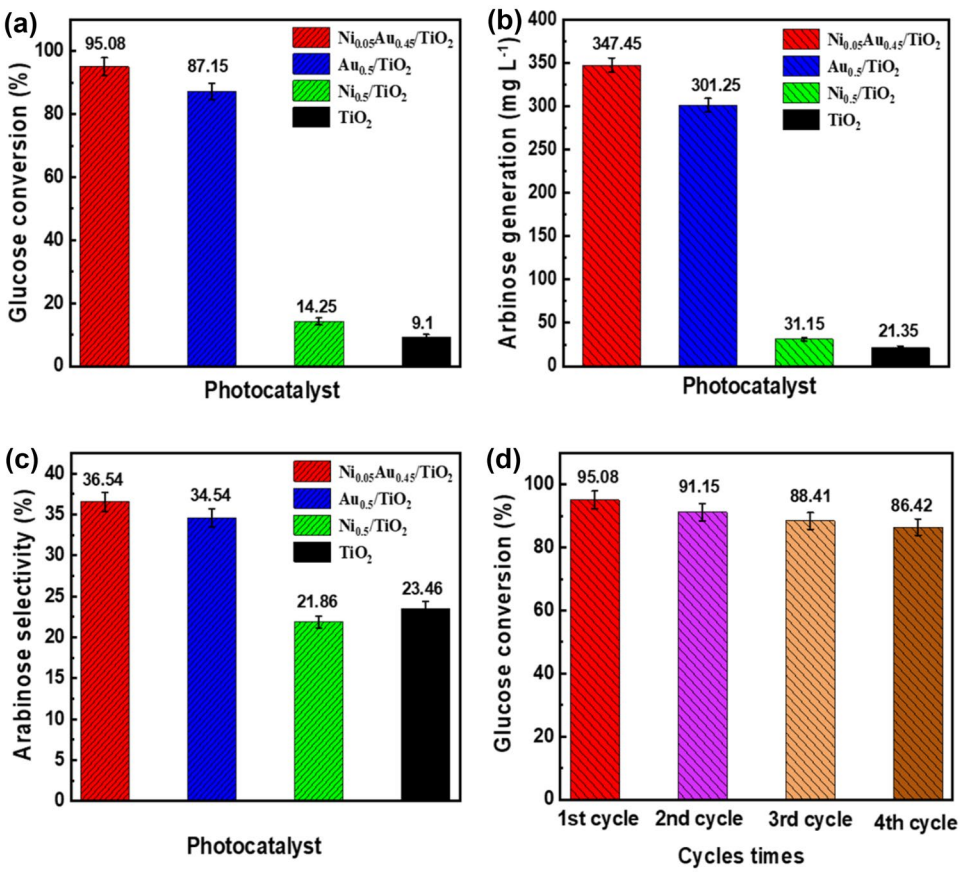


**Fig. 5** **a** Glucose conversion, **b** arabinose generation, and **c** arabinose selectively of different catalysts; **d** long time recycling test of the optimal system for glucose conversion. Reaction condition: 25 mg catalyst, 25 mL $H_2O$, 25 mL $CNCH_3$, 6 mmol $L^{-1}$ $Na_2CO_3$, 50 mg glucose, 300 W Xenon lamp

$h^{-1}$ $g^{-1}$), respectively. Such excellent $H_2$ evolution activity of $Ni_{0.05}Au_{0.45}/TiO_2$ was not only related to the properties of $TiO_2$ itself (the Ov and 3D hierarchical urchin-like morphology), but also more attributable to the modification of Ni and Au NPs with the synergetic effect. Firstly, Au NPs LSPR greatly promotes the light absorption by the catalyst, resulting in excited photogenerated $e^-$-$h^+$ for photoreforming reaction [55, 61]. Secondly, a Schottky contact could be formed between $TiO_2$ and Ni NPs and between $TiO_2$ and Au NPs with a high work function ($Au_\Phi$ = 5.3–5.6 eV, $Ni_\Phi$ = 5.3 eV), where $e^-$ could be transferred from the CB of $TiO_2$ to Ni and Au NPs for $H^+$ reduction, but not back [17, 62].

The stability and versatility also matter much for a photoreforming system. As shown in Fig. 4c, the $H_2$ production efficiency slightly decreased after 5 cycles, which might be owing to the Ni and Au NPs partially dislodged during the washing process and the fracture of the 1D nanorods in $TiO_2$. The versatility of the system was carried out by photoreforming different biomass derivatives (e.g., cellobiose, glucose, α-cellulose, xylose, galactose, and fructose) under the same conditions (Fig. 4f). It could be clearly seen that the monosaccharides with simpler structures (e.g., glucose, galactose, fructose) exhibited a higher $H_2$ production rate than other saccharides (such as saccharose, xylan, and α-Cellulose). It was worth mentioning that $Ni_{0.05}Au_{0.45}/TiO_2$ showed relatively good $H_2$ generation activity even for high crystallinity α-cellulose without any pretreatment under weak alkaline conditions (6 mmol $L^{-1}$ $Na_2CO_3$), which demonstrated the potential of $Ni_xAu_{0.5-x}/TiO_2$ in the photoreforming field. The $H_2$ evolution performance of $Ni_{0.05}Au_{0.45}/TiO_2$ was comparable to other $TiO_2$-based catalysts reported in the literatures (Fig. 6a and Table S2).

### 3.4 Photoreforming for arabinose production

What's charming of the photoreforming reaction is that the value-added chemicals can be generated, while producing a clean fuel $H_2$ under the solar radiation [55]. Here, the liquid phase products of $TiO_2$ and $Ni_xAu_{0.5-x}/TiO_2$ and control system were assessed, and the dominant liquid phase product was arabinose within the detection limit of high-performance liquid chromatography (HPLC, Agilent 1290 Infinity II). The glucose conversion ratio of isolated $TiO_2$ was determined to be around 9.1% and the arabinose selectivity was 23.46% after 4-h photoreforming reaction (Fig. 5a–c). As discussed before, the introduction of $O_v$ triggered by $Ti^{3+}$ doping and the sufficient contact between the photocatalyst and the

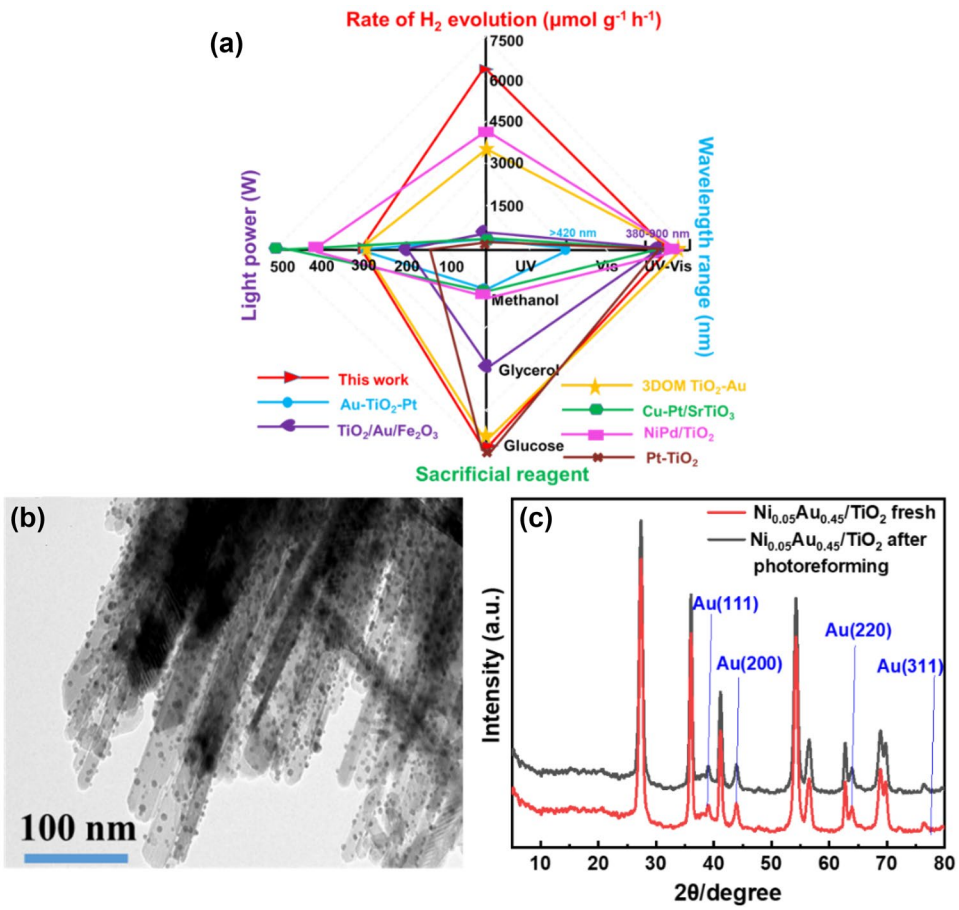


**Fig. 6** **a** The comparison of $H_2$ generation activity for the $Ni_{0.05}Au_{0.45}/TiO_2$ and some reported $TiO_2$-based photocatalysts (all details were described in Table S2 in the Supporting Information). **b** HRTEM of $Ni_{0.05}Au_{0.45}/TiO_2$ after photoreforming. **c** PXRD of $Ni_{0.05}Au_{0.45}/TiO_2$ fresh and after photoreforming

glucose substrate because of the unique 3D hierarchical urchin-like morphology in $TiO_2$ is pivotal in arabinose production by photoreforming [55, 61]. As expected, the $Ni_{0.05}Au_{0.45}/TiO_2$ demonstrated a high glucose conversion of 95.08% after 4-h photoreforming reaction, while $Au_{0.5}/TiO_2$ and $Ni_{0.5}/TiO_2$ gave a glucose conversion of 87.15%, and 14.25%, respectively (Fig. 5a). The arabinose selectivity (Fig. 5b) after photoreforming of these catalysts also maintained the same trend, that was, $Ni_{0.05}Au_{0.45}/TiO_2$ (36.54%), $Au_{0.5}/TiO_2$ (34.56%), $Ni_{0.5}/TiO_2$ (21.86%). These results further confirmed the synergistic effect of Au and Ni bimetallic NPs in the photoreforming process. In addition to the LSPR of Au NPs and the Schottky contact between $TiO_2$ and Au/Ni NPs, we speculated that the ability of Ni NPs in C–C bonds cleavage in glucose also played a vital role in the photoreforming [21]. Moreover, the arabinose concentration for $Ni_{0.05}Au_{0.45}/TiO_2$ system after 4 h photoreforming could be as high as 347.45 mg $L^{-1}$, which was 1.15, 11.15, and 16.27 times that of $Au_{0.5}/TiO_2$ (301.25 mg $L^{-1}$), $Ni_{0.5}/TiO_2$ (31.15 mg $L^{-1}$) and $TiO_2$ (21.35 mg $L^{-1}$), respectively (Fig. 5c).

Furthermore, glucose conversion of $Ni_{0.05}Au_{0.45}/TiO_2$ in cyclic experiments was studied (Fig. 5d). It could be found that the glucose conversion was maintained above 85% after 4 cycles of measurement, which proved the good cycling stability of photocatalyst. And the TEM images and pXRD patterns of $Ni_{0.05}Au_{0.45}/TiO_2$ before and after 4 h photoreforming was shown in Fig. 6b, c, which proved the morphology and structural stability of $Ni_{0.05}Au_{0.45}/TiO_2$.

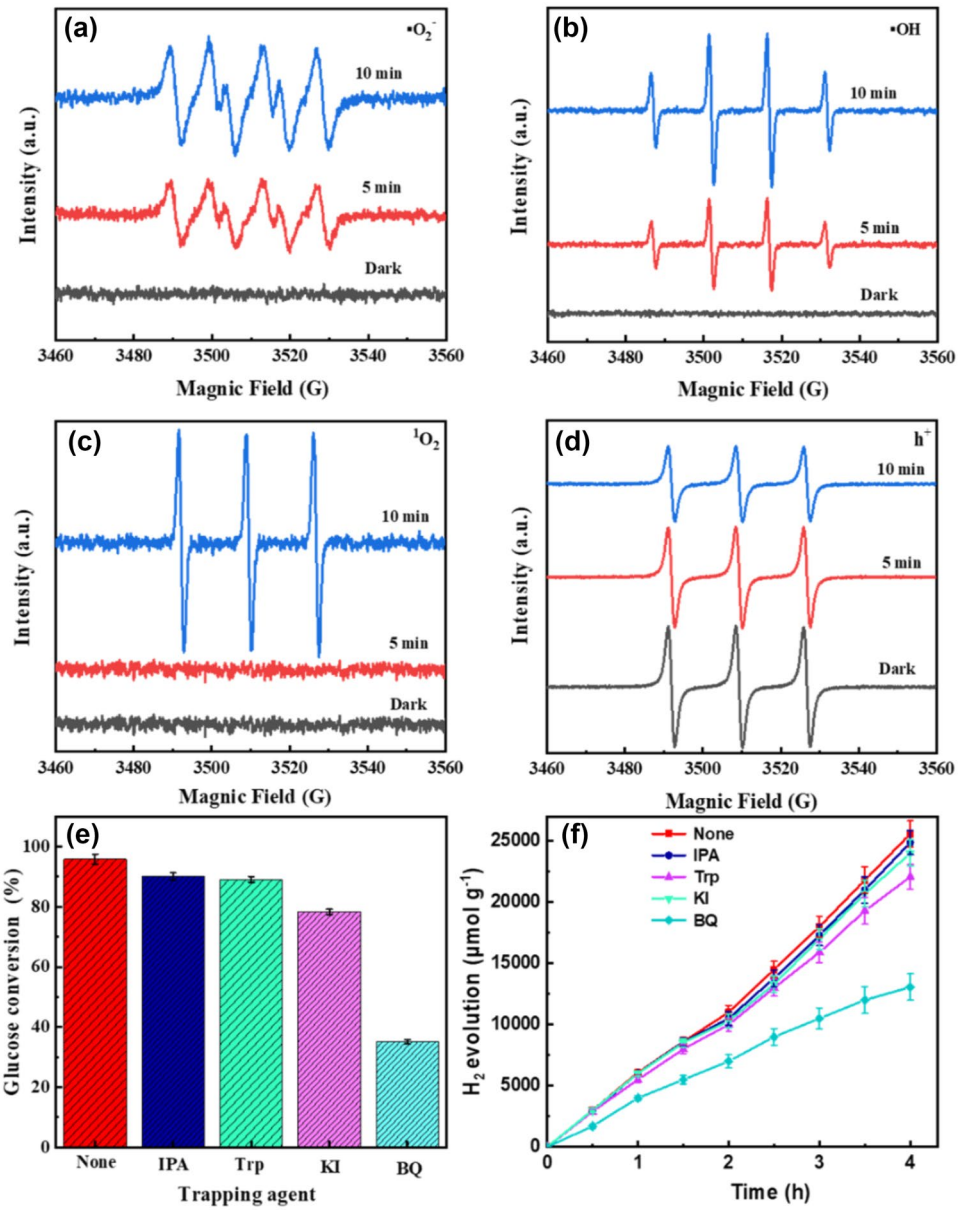


**Fig. 7** DMPO ESR spin-labeling for **a** $\bullet O^{2-}$ and **b** $\bullet$OH; **c** TEMP ESR for spin-labeling $^1O_2$; **d** TEMPO ESR spin-labeling for $h^+$; **e** glucose convention rare; **f** $H_2$ production

### 3.5 Mechanism investigation

To better understand the glucose photoreforming mechanism for the enhanced coproduction of $H_2$ and arabinose over $Ni_{0.05}Au_{0.45}/TiO_2$, the detection of reactive species ($\bullet O^{2-}$, $\bullet OH$, $^1O_2$, and $h^+$) was executed by electron spin resonance (ESR). 5,5′-Dimethyl-1-pyrroline N-oxide (DMPO), 2, 2, 6, 6-tetramethylpiperidine (TEMP), and 2, 2, 6, 6-tetramethylpiperidinooxy (TEMPO) were used as the spin traps for $\bullet O^{2-}$ and $\bullet OH$, $^1O_2$, and $h^+$, respectively. As shown in Fig. 7a, b, no ESR signal of $\bullet O^{2-}$ and $\bullet OH$ was observed in the system under dark conditions. When the optimal system was under illumination, both $\bullet O^{2-}$ and $\bullet OH$ were generated and they reacted with DMPO to present the typical ESR signals. Moreover, the ESR signals were enhanced gradually as the irradiation time increases. The change trend of $^1O_2$ was consistent with the $\bullet O^{2-}$ and $\bullet OH$. Three typical signals of $^1O_2$ with 1:1:1 relative intensity appeared with the extension of irradiation time (Fig. 7c). As for $h^+$ detection, it was observed from Fig. 7d, the TEMPO characteristic peaks with a relative intensity of 1:1:1 were observed under dark. Once the system was exposed to light, TEMPO would combine with $e^-$ produced by the photocatalyst to form TEMPOH, the ESR signal of TEMPO was weakened. More $e^-$ were produced in the system, the lower the signal peak intensity would be. Since $e^-$ and $h^+$ were generated in pairs during the photoreforming process, the ESR signal of the $h^+$ was consistent with that of $e^-$.

The main oxidative species in glucose photoreforming were studied by quenching experiments. Isopropanol (IPA), tryptophan (Trp), KI, and benzoquinone (BQ) were applied in the optimum system as sacrificial agents to consume $\bullet OH$, $^1O_2$, $h^+$, and $\bullet O^{2-}$, respectively. As observed in Fig. 7e, the glucose conversion was inhibited in the presence of IPA (5.78%), Trp (6.68%), KI (17.50%), and BQ (60.75%), which indicated that the effect of $\bullet OH$, $^1O_2$, $h^+$, and $\bullet O^{2-}$ on facilitating the photoreforming reaction was in turn improved. According to the band structure analysis of $Ni_{0.05}Au_{0.45}/TiO_2$ in Sect. 3.2, the $E_{VB}$ of $Ni_{0.05}Au_{0.45}/TiO_2$ (+2.34 V vs. NHE) was more positive than $OH^-/\bullet OH$ (1.90 eV vs. NHE), so the $\bullet OH$ was produced by this route. Meanwhile, the $E_{CB}$ of $Ni_{0.05}Au_{0.45}/TiO_2$ (−0.52 V vs. NHE) was more negative than $O_2/\bullet O^{2-}$ ($E^\theta = -0.69$ eV vs. NHE), $\bullet O^{2-}$ could be obtained. Furthermore, the $^1O_2$ could be produced by oxidizing $h^+$. This was further validated the ESR analysis. Figure 7f reveals the $H_2$ production activity under different trapping agents; the result was coincident with Fig. 7e.

A plausible explanation for the significant increase in $H_2$ and arabinose co-generation and glucose conversion over $Ni_{0.05}Au_{0.45}/TiO_2$ was proposed based on our results and some previous works [55, 63, 64] (Fig. 8). Under visible irradiation, the $h^+$-$e^-$ was produced by $TiO_2$, and then the $e^-$ was transferred from CB of $TiO_2$ to Au and Ni NPs for the

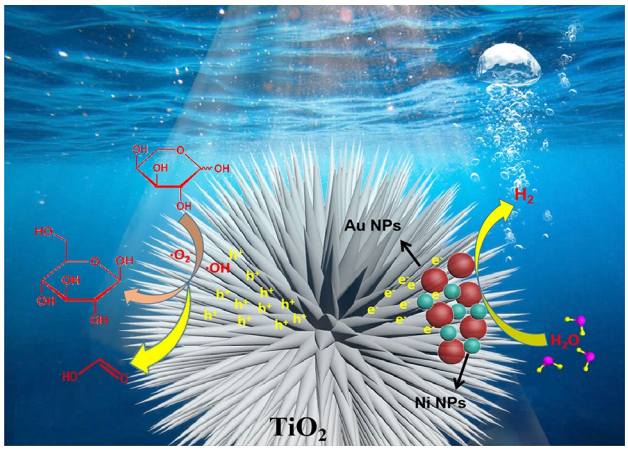


**Fig. 8** The illustration of $H_2$ and arabinose production by glucose photoreforming over $Ni_{0.05}Au_{0.45}/TiO_2$

$H_2$ production by $H^+$ reduction. In the meanwhile, glucose was oxidized to produce gluconic acid by $\bullet O^{2-}$ [4]. Gluconic acid was subsequently decarboxylated through C1-C2 α-scissions due to the promoting effect of Ni NPs on the C–C cleavage, resulting in the formation of arabinose and formic acid [61]. But no formic acid was detected, which possibly because it was dehydrated in the subsequent reaction, and CO was produced [12].

## 4 Conclusions

In summary, a high-efficiency photocatalyst $Ni_xAu_{1-x}/TiO_2$ has been successfully synthesized for $H_2$ and arabinose coproduction by glucose photoreforming. Au NPs with localized surface plasmon resonance (LSPR) effect and high work function significantly facilitated the separation of photogenerated carriers; the transition metal Ni NPs with low coat and high work function ($Ni_\Phi = 5.3$ eV) promoted C–C bond cleavage. The $Ni_xAu_{0.5-x}/TiO_2$ obtained by one-step impregnation showed the prominent photoreforming activity by fully exerting the synergistic effect of Ni and Au NPs. Under optimal conditions, the $H_2$ production rate of 6391.86 μmol $h^{-1}$ $g^{-1}$, 95.00% glucose conversion, and 36.54% arabinose selectivity could be achieved on $Ni_{0.05}Au_{0.45}/TiO_2$. The enhanced photoreforming activity could be attributed to the synergistic effect of Ni and Au NPs, including the localized surface plasmon resonance (LSPR) and Schottky junction of Au nanoparticles and the promoting effect of Ni particles on C–C cleavage in glucose, as well as the glucose accessibility caused by the 3D hierarchical urchin-like $TiO_2$. The photoreforming mechanism showed that $\bullet O_2^-$ plays an important role in the glucose oxidation. Glucose was converted to gluconic acid by $\bullet O_2^-$. Gluconic acid was subsequently decarboxylated through C1-C2 α-scissions, resulting

in the formation of arabinose and formic acid. This work demonstrates a feasible way to sustainable coproduction of $H_2$ and chemicals, which would be a very robust alternative in biomass photoreforming systems.

**Supplementary Information** The online version contains supplementary material available at https://doi.org/10.1007/s42114-022-00580-6.

**Author contribution** Malin Eqi and Cai Shi wrote the main manuscript text; Jiajing Xie, Fuyan Kang, Houjuan Qi, and Xushen Tan prepared Scheme 1, Figs. 1–8, and Figs. S1–S4. All authors reviewed the manuscript.

**Funding** This work was supported by the National Natural Science Foundation of China (No. 32071713), the Outstanding Youth Foundation Project of Heilongjiang Province (No. JQ2019C001), the Natural Science Basic Research Program of Shaanxi (Grant No. 2022JQ-441), and the Central University Basic Scientifc Research Project of China (No. 2572020DX01).

## Declarations

**Conflict of interest** The authors declare no competing interests.

## References

1. Zhao H, Li CF, Yong X, Kumar P, Palma B, Hu ZY, Van Tendeloo G, Siahrostami S, Larter S, Zheng D, Wang S, Chen Z, Kibria MG, Hu J (2021) Coproduction of hydrogen and lactic acid from glucose photocatalysis on band-engineered $Zn_{1-x}Cd_xS$ homojunction. iScience 24:102109–102120. https://doi.org/10.1016/j.isci.2021.102109
2. Pan D, Su F, Liu H, Liu C, Umar A, Castañeda L, Algadi H, Wang C, Guo Z (2021) Research progress on catalytic pyrolysis and reuse of waste plastics and petroleum sludge. ES Mater Manuf 11:3–15. https://doi.org/10.30919/esmm5f415
3. Ragauskas AJ, Williams CK, Davison BH, Britovsek G, Cairney J, Eckert CA, Frederick WJ Jr, Hallett JP, Leak DJ, Liotta CL, Mielenz JR, Murphy R, Templer R, Tschaplinski T (2006) The path forward for biofuels and biomaterials. Science 311:484–489. https://doi.org/10.1126/science.1114736
4. Zhao H, Liu P, Wu X, Wang A, Zheng D, Wang S, Chen Z, Larter S, Li Y, Su B-L, Kibria MG, Hu J (2021) Plasmon enhanced glucose photoreforming for arabinose and gas fuel co-production over 3DOM $TiO_2$-Au. Appl Catal B Environ 291:120055–120064. https://doi.org/10.1016/j.apcatb.2021.120055
5. Kuehnel MF, Reisner E (2018) Solar hydrogen generation from lignocellulose. Angew Chem Int Ed Engl 57:3290–3296. https://doi.org/10.1002/anie.201710133
6. Caravaca A, Jones W, Hardacre C, Bowker M (2016) $H_2$ production by the photocatalytic reforming of cellulose and raw biomass using Ni, Pd, Pt and Au on titania. Proc Math Phys Eng Sci 472:20160054–20160065. https://doi.org/10.1098/rspa.2016.0054
7. Liu WJ, Xu Z, Zhao D, Pan XQ, Li HC, Hu X, Fan ZY, Wang WK, Zhao GH, Jin S, Huber GW, Yu HQ (2020) Efficient electrochemical production of glucaric acid and $H_2$ via glucose electrolysis. Nat Commun 11:265–276. https://doi.org/10.1038/s41467-019-14157-3
8. Zhang Z, Huber GW (2018) Catalytic oxidation of carbohydrates into organic acids and furan chemicals. Chem Soc Rev 47:1351–1390. https://doi.org/10.1039/c7cs00213k
9. Zhang P, Sun D, Cho A, Weon S, Lee S, Lee J, Han JW, Kim DP, Choi W (2019) Modified carbon nitride nanozyme as bifunctional glucose oxidase-peroxidase for metal-free bioinspired cascade photocatalysis. Nat Commun 10:940–954. https://doi.org/10.1038/s41467-019-08731-y
10. Zhou B, Song J, Wu T, Liu H, Xie C, Yang G, Han B (2016) Simultaneous and selective transformation of glucose to arabinose and nitrosobenzene to azoxybenzene driven by visible-light. Green Chem 18:3852–3857. https://doi.org/10.1039/c6gc00943c
11. Sanwald KE, Berto TF, Eisenreich W, Jentys A, Gutiérrez OY, Lercher JA (2017) Overcoming the rate-limiting reaction during photoreforming of sugar aldoses for $H_2$-generation. ACS Catal 7:3236–3244. https://doi.org/10.1021/acscatal.7b00508
12. Chong R, Li J, Ma Y, Zhang B, Han H, Li C (2014) Selective conversion of aqueous glucose to value-added sugar aldose on $TiO_2$-based photocatalysts. J Catal 314:101–108. https://doi.org/10.1016/j.jcat.2014.03.009
13. Zhao Y, Zeng Q, Feng T, Xia C, Liu C, Yang F, Zhang K, Yang B (2019) Carbonized polymer dots/$TiO_2$ photonic crystal heterostructures with enhanced light harvesting and charge separation for efficient and stable photocatalysis. Mater Chem Front 3:2659–2667. https://doi.org/10.1039/c9qm00556k
14. Silva CG, Sampaio MJ, Marques RRN, Ferreira LA, Tavares PB, Silva AMT, Faria JL (2015) Photocatalytic production of hydrogen from methanol and saccharides using carbon nanotube-$TiO_2$ catalysts. Appl Catal B Environ 178:82–90. https://doi.org/10.1016/j.apcatb.2014.10.032
15. Yu X, Fan X, An L, Liu G, Li Z, Liu J, Hu P (2018) Mesocrystalline $Ti^{3+}$ $TiO_2$ hybridized g-$C_3N_4$ for efficient visible-light photocatalysis. Carbon 128:21–30. https://doi.org/10.1016/j.carbon.2017.11.078
16. Roongraung K, Chuangchote S, Laosiripojana N, Sagawa T (2020) Electrospun Ag-$TiO_2$ nanofibers for photocatalytic glucose conversion to high-value chemicals. ACS Omega 5:5862–5872. https://doi.org/10.1021/acsomega.9b04076
17. Luna AL, Dragoe D, Wang K, Beaunier P, Kowalska E, Ohtani B, Bahena Uribe D, Valenzuela MA, Remita H, Colbeau-Justin C (2017) Photocatalytic hydrogen evolution using Ni–Pd/$TiO_2$: correlation of light absorption, charge-carrier dynamics, and quantum efficiency. J Phy Chem C 121:14302–14311. https://doi.org/10.1021/acs.jpcc.7b01167
18. Shi C, Yuan W, Qu K, Shi J, Eqi M, Tan X, Huang Z, Gándara F, Pan D, Naik N, Zhang Y, Guo Z (2021) Gold/titania nanorod assembled urchin-like photocatalysts with an enhanced hydrogen generation by photocatalytic biomass reforming. Eng Sci 16:374–386. https://doi.org/10.30919/es8d478
19. Zhao H, Li CF, Liu LY, Palma B, Hu ZY, Renneckar S, Larter S, Li Y, Kibria MG, Hu J, Su BL (2021) n-p Heterojunction of $TiO_2$-NiO core-shell structure for efficient hydrogen generation and lignin photoreforming. J Colloid Interface Sci 585:694–704. https://doi.org/10.1016/j.jcis.2020.10.049
20. Davda RR, Shabaker JW, Huber GW, Cortright RD, Dumesic JA (2005) A review of catalytic issues and process conditions for renewable hydrogen and alkanes by aqueous-phase reforming of oxygenated hydrocarbons over supported metal catalysts. Appl Catal B Environ 56:171–186. https://doi.org/10.1016/j.apcatb.2004.04.027
21. Zhang J, Zhu Y, An Z, Shu X, Ma X, Song H, Wang W, He J (2020) Size effects of Ni particles on the cleavage of C-H and C–C bonds toward hydrogen production from cellulose. ACS Appl Energy Mater 3:7048–7057. https://doi.org/10.1021/acsaem.0c01104
22. Kalisman P, Houben L, Aronovitch E, Kauffmann Y, Bar-Sadan M, Amirav L (2015) The golden gate to photocatalytic hydrogen production. J Mater Chem A 3:19679–19682. https://doi.org/10.1039/c5ta05784a
23. Zheng X, Shen G, Wang C, Li Y, Dunphy D, Hasan T, Brinker CJ, Su BL (2017) Bio-inspired murray materials for mass transfer and

activity. Nat Commun 8:14921–14930. https://doi.org/10.1038/ncomms14921
24. Tudu B, Nalajala N, Saikia P, Gopinath CS (2020) Cu–Ni Bimetal Integrated $TiO_2$ Thin film for enhanced solar hydrogen generation. Sol RRL 4:1900557–1900567. https://doi.org/10.1002/solr.201900557
25. Wang Y, Zhang S, Huang C, Qu F, Yao D, Guo H, Xu H, Jiang C, Yang M (2021) Mesoporous WO3 modified by Au nanoparticles for enhanced trimethylamine gas sensing properties. Dalton Trans 50:970–978
26. Wang Y, Zhang S, Huang C, Qu F, Yao D, Guo H, Xu H, Jiang C, Yang M (2021) Mesoporous $WO_3$ modified by Au nanoparticles for enhanced trimethylamine gas sensing properties. Dalton T 50:970–978. https://doi.org/10.1039/d0dt03131c
27. Yu X, Fan X, Li Z, Liu J (2017) Synthesis of plasmonic $Ti^{3+}$ doped Au/Cl-$TiO_2$ mesocrystals with enhanced visible light photocatalytic activity. Dalton T 46:11898–11904. https://doi.org/10.1039/c7dt02824e
28. Yu Y, Dong X, Chen P, Geng Q, Wang H, Li J, Zhou Y, Dong F (2021) Synergistic effect of Cu single atoms and Au-Cu alloy nanoparticles on $TiO_2$ for efficient $CO_2$ photoreduction. ACS Nano 15:14453–14464. https://doi.org/10.1021/acsnano.1c03961
29. Qin L, Si G, Li X, Kang S-Z (2015) Synergetic effect of Cu–Pt bimetallic cocatalyst on $SrTiO_3$ for efficient photocatalytic hydrogen production from water. RSC Adv 5:102593–102598. https://doi.org/10.1039/c5ra22757g
30. Patra KK, Gopinath CS (2016) Bimetallic and plasmonic Ag-Au on $TiO_2$ for solar water splitting: an active nanocomposite for entire visible-light-region absorption. ChemCatChem 8:3294–3311. https://doi.org/10.1002/cctc.201600937
31. Bharad PA, Sivaranjani K, Gopinath CS (2015) A rational approach towards enhancing solar water splitting: a case study of Au-RGO/N-RGO-$TiO_2$. Nanoscale 7:11206–11215. https://doi.org/10.1039/c5nr02613j
32. Sivaranjani K, RajaAmbal S, Das T, Roy K, Bhattacharyya S, Gopinath CS (2014) Disordered mesoporous $TiO_{2-x}N_x$ nano-Au: an electronically integrated nanocomposite for solar $H_2$ generation. ChemCatChem 6:522–530. https://doi.org/10.1002/cctc.201300715
33. Tudu B, Nalajala N, Reddy KP, Saikia P, Gopinath CS (2019) Electronic integration and thin film aspects of Au-Pd/rGO/$TiO_2$ for improved solar hydrogen generation. ACS Appl Mater Interfaces 11:32869–32878. https://doi.org/10.1021/acsami.9b07070
34. Yan Y, Xia BY, Zhao B, Wang X (2016) A review on noble-metal-free bifunctional heterogeneous catalysts for overall electrochemical water splitting. J Mater Chem A 4:17587–17603. https://doi.org/10.1039/c6ta08075h
35. Xu J, Li M, Yang L, Qiu J, Chen Q, Zhang X, Feng Y, Yao J (2020) Synergy of Ni dopant and oxygen vacancies in ZnO for efficient photocatalytic depolymerization of sodium lignosulfonate. Chem Eng J 394:125050–125070. https://doi.org/10.1016/j.cej.2020.125050
36. Jiang B, Tang Y, Qu Y, Wang JQ, Xie Y, Tian C, Zhou W, Fu H (2015) Thin carbon layer coated $Ti^{3+}$-$TiO_2$ nanocrystallites for visible-light driven photocatalysis. Nanoscale 7:5035–5045. https://doi.org/10.1039/c5nr00032g
37. Fang W, Xing M, Zhang J (2014) A new approach to prepare $Ti^{3+}$ self-doped $TiO_2$ via $NaBH_4$ reduction and hydrochloric acid treatment. Appl Catal B Environ 160:240–246. https://doi.org/10.1016/j.apcatb.2014.05.031
38. Xing M, Fang W, Nasir M, Ma Y, Zhang J, Anpo M (2013) Self-doped $Ti^{3+}$ -enhanced $TiO_2$ nanoparticles with a high-performance photocatalysis. J Catal 297:236–243. https://doi.org/10.1016/j.jcat.2012.10.014
39. Guo F, Sun H, Cheng L, Shi W (2020) Oxygen-defective ZnO porous nanosheets modified by carbon dots to improve their visible-light photocatalytic activity and gain mechanistic insight. New J Chem 44:11215–11223. https://doi.org/10.1039/d0nj02268c
40. Geng Z, Kong X, Chen W, Su H, Liu Y, Cai F, Wang G, Zeng J (2018) Oxygen vacancies in ZnO nanosheets enhance $CO_2$ electrochemical reduction to CO. Angew Chem Int Ed Engl 57:6054–6059. https://doi.org/10.1002/anie.201711255
41. Nowotny J, Alim MA, Bak T, Idris MA, Ionescu M, Prince K, Sahdan MZ, Sopian K, Mat Teridi MA, Sigmund W (2015) Defect chemistry and defect engineering of $TiO_2$-based semiconductors for solar energy conversion. Chem Soc Rev 44:8424–8442. https://doi.org/10.1039/c4cs00469h
42. Zhang B, Wang L, Zhang Y, Ding Y, Bi Y (2018) Ultrathin FeOOH nanolayers with abundant oxygen vacancies on $BiVO_4$ photoanodes for efficient water oxidation. Angew Chem Int Ed Engl 57:2248–2252. https://doi.org/10.1002/anie.201712499
43. Zhang Y, Xu Z, Li G, Huang X, Hao W, Bi Y (2019) Direct observation of oxygen vacancy self-healing on $TiO_2$ photocatalysts for solar water splitting. Angew Chem Int Ed Engl 58:14229–14233. https://doi.org/10.1002/anie.201907954
44. Li C, Wang T, Zhao ZJ, Yang W, Li JF, Li A, Yang Z, Ozin GA, Gong J (2018) Promoted fixation of molecular nitrogen with surface oxygen vacancies on plasmon-enhanced $TiO_2$ photoelectrodes. Angew Chem Int Ed Engl 57:5278–5282. https://doi.org/10.1002/anie.201713229
45. Yu H, Li J, Zhang Y, Yang S, Han K, Dong F, Ma T, Huang H (2019) Three-in-one oxygen vacancies: whole visible-spectrum absorption, efficient charge separation, and surface site activation for robust $CO_2$ photoreduction. Angew Chem Int Ed Engl 58:3880–3884. https://doi.org/10.1002/anie.201813967
46. Chowdhury IH, Roy M, Kundu S, Naskar MK (2019) $TiO_2$ hollow microspheres impregnated with biogenic gold nanoparticles for the efficient visible light-induced photodegradation of phenol. J Phys Chem Solids 129:329–339. https://doi.org/10.1016/j.jpcs.2019.01.036
47. Kang F, Shi C, Li W, Eqi M, Liu Z, Zheng X, Huang Z (2022) Honeycomb like CdS/sulphur-modified biochar composites with enhanced adsorption-photocatalytic capacity for effective removal of rhodamine B. J Environ Chem Eng 10:106942–106953. https://doi.org/10.1016/j.jece.2021.106942
48. Lin Z, Du C, Yan B, Wang C, Yang G (2018) Two-dimensional amorphous NiO as a plasmonic photocatalyst for solar H2 evolution. Nat Commun 9:4036
49. Vinesh V, Shaheer ARM, Neppolian B (2019) Reduced graphene oxide (rGO) supported electron deficient B-doped $TiO_2$ (Au/B-$TiO_2$/rGO) nanocomposite: an efficient visible light sonophotocatalyst for the degradation of tetracycline (TC). Ultrason Sonochem 50:302–310. https://doi.org/10.1016/j.ultsonch.2018.09.030
50. Makula P, Pacia M, Macyk W (2018) How to correctly determine the band gap energy of modified semiconductor photocatalysts based on UV-Vis spectra. J Phys Chem Lett 9:6814–6817. https://doi.org/10.1021/acs.jpclett.8b02892
51. Valan MF, Manikandan A, Antony SA (2015) A novel synthesis and characterization studies of magnetic $Co_3O_4$ nanoparticles. J Nanosci Nanotechnol 15:4580–4586. https://doi.org/10.1166/jnn.2015.9776
52. Quesada-Cabrera R, Sotelo-Vazquez C, Bear JC, Darr JA, Parkin IP (2014) Photocatalytic evidence of the rutile-to-anatase electron transfer in titania. Adv Mater Interfaces 1:1400069–1400076. https://doi.org/10.1002/admi.201400069
53. Nosaka Y, Nosaka AY (2016) Reconsideration of intrinsic band alignments within anatase and rutile $TiO_2$. J Phys Chem Lett 7:431–434. https://doi.org/10.1021/acs.jpclett.5b02804
54. Scanlon DO, Dunnill CW, Buckeridge J, Shevlin SA, Logsdail AJ, Woodley SM, Catlow CR, Powell MJ, Palgrave RG, Parkin IP, Watson GW, Keal TW, Sherwood P, Walsh A, Sokol AA (2013)

Band alignment of rutile and anatase $TiO_2$. Nat Mater 12:798–801. https://doi.org/10.1038/nmat3697
55. Zhao H, Yu X, Li C-F, Yu W, Wang A, Hu Z-Y, Larter S, Li Y, Golam Kibria M, Hu J (2022) Carbon quantum dots modified $TiO_2$ composites for hydrogen production and selective glucose photoreforming. J Energy Chem 64:201–208. https://doi.org/10.1016/j.jechem.2021.04.033
56. Di J, Xia J, Yin S, Xu H, Xu L, Xu Y, He M, Li H (2014) Preparation of sphere-like g-$C_3N_4$/BiOI photocatalysts via a reactable ionic liquid for visible-light-driven photocatalytic degradation of pollutants. J Mater Chem A 2:5340–5351. https://doi.org/10.1039/c3ta14617k
57. Yang M-Q, Han C, Xu Y-J (2015) Insight into the effect of highly dispersed $MoS_2$ versus layer-structured $MoS_2$ on the photocorrosion and photoactivity of CdS in graphene–CdS–$MoS_2$ composites. J Phys Chem C 119:27234–27246. https://doi.org/10.1021/acs.jpcc.5b08016
58. Shi C, Qi H, Sun Z, Qu K, Huang Z, Li J, Dong M, Guo Z (2020) Carbon dot-sensitized urchin-like $Ti^{3+}$ self-doped $TiO_2$ photocatalysts with enhanced photoredox ability for highly efficient removal of $Cr^{6+}$ and RhB. J Mate Chem C 8:2238–2247. https://doi.org/10.1039/c9tc05513d
59. Bai Y, Ye L, Chen T, Wang L, Shi X, Zhang X, Chen D (2016) Facet-dependent photocatalytic $N_2$ fixation of bismuth-rich $Bi_5O_7I$ nanosheets. ACS Appl Mater Interfaces 8:27661–27668. https://doi.org/10.1021/acsami.6b08129
60. Abdouli I, Eternot M, Dappozze F, Guillard C, Essayem N (2021) Comparison of hydrothermal and photocatalytic conversion of glucose with commercial $TiO_2$: superficial properties-activities relationships. Catal Today 367:268–277. https://doi.org/10.1016/j.cattod.2020.03.040
61. Da Già L, Recchi C, Gonzalez-Yañez EO, Davies TE, Lopez-Sanchez JA (2017) Visible light selective photocatalytic conversion of glucose by $TiO_2$. Appl Catal B Environ 202:281–288. https://doi.org/10.1016/j.apcatb.2016.08.035
62. Chen W-T, Chan A, Sun-Waterhouse D, Llorca J, Idriss H, Waterhouse GIN (2018) Performance comparison of Ni/$TiO_2$ and Au/$TiO_2$ photocatalysts for $H_2$ production in different alcohol-water mixtures. J Catal 367:27–42. https://doi.org/10.1016/j.jcat.2018.08.015
63. Bellardita M, García-López EI, Marcì G, Palmisano L (2016) Photocatalytic formation of $H_2$ and value-added chemicals in aqueous glucose (Pt)-$TiO_2$ suspension. Int J Hydrogen Energ 41:5934–5947. https://doi.org/10.1016/j.ijhydene.2016.02.103
64. Bahadori E, Ramis G, Zanardo D, Menegazzo F, Signoretto M, Gazzoli D, Pietrogiacomi D, Michele AD, Rossetti I (2020) Photoreforming of glucose over CuO/$TiO_2$. Catalysts 10:477–497. https://doi.org/10.3390/catal10050477